Nonlinear plasma-assisted collapse of ring-Airy wave packets

Paris Panagiotopoulos, Arnaud Couairon, Miroslav Kolesik, Dimitris G. Papazoglou, Jerome V. Moloney, and Stelios Tzortzakis

Phys. Rev. A **93**, 033808 — Published 3 March 2016

DOI: 10.1103/PhysRevA.93.033808

Nonlinear plasma assisted collapse of ring-Airy wavepackets

Paris Panagiotopoulos[1,2], Arnaud Couairon[3], Miroslav Kolesik[1,2], Dimitris G. Papazoglou[4,5], Jerome V. Moloney[1,2,6], and Stelios Tzortzakis[4,5,7]

[1] Arizona Center for Mathematical Sciences, University of Arizona, Tucson 85721-0094

[2] College of Optical Sciences, University of Arizona, Tucson 85721-0094

[3] Centre de Physique Théorique, Ecole polytechnique, CNRS, Université Paris-Saclay, F-91128 Palaiseau, France

[4] Institute of Electronic Structure and Laser, Foundation for Research and Technology Hellas, PO Box 1527, 71110 Heraklion, Greece

[5] Materials Science and Technology Department, University of Crete, PO Box 2208, 71003 Heraklion, Greece

[6] Department of Mathematics, University of Arizona, Tucson 85721-0094

[7] Science Program, Texas A&M University at Qatar, P.O. Box 23874 Doha, Qatar

We numerically demonstrate that femtosecond ring-Airy wavepackets are able to overcome the reference intensity clamping of 4×10^{13} W/cm^2 for filaments generated with Gaussian beams at low numerical apertures, and form an intense sharp intensity peak on-axis. Numerical simulations, with unidirectional propagation models for the pulse envelope and the carrier resolved electric field, reveal that the driving mechanism for this unexpected intensity increase is due to the self-generated plasma. The plasma formation, in conjunction with the circular geometry of the beam, force the wavepacket into a multi-stage collapse process which takes place faster than the saturating mechanisms can compensate. This is to our knowledge the first report of a non-standard mechanism increasing the intensity of a collapsing wavepacket, due to the joint contributions of the cubic phase of the Airy beam and the formation of a partially reflecting plasma.

I. INTRODUCTION

The continuing quest to reach higher laser intensities has always been a fundamental aspect of nonlinear optics, since by definition nonlinear processes vary in a nonlinear way to the applied electric field amplitude. Virtually the entirety of the field of nonlinear optics studies effects that are either directly or indirectly related to laser intensity, such as pulse compression [1, 2], carrier wave shock formation [3–5], higher harmonic generation [6], and THz radiation generation [7], just to name a few.

However in practical applications there are limitations on achievable intensities due to saturating effects, which are in principle of a higher order, such as optical field ionization, that dominate the propagation once intensity reaches a certain threshold value. Any advance in increasing or controlling laser intensities in a given setting will have tremendous impact in multiple applications in nonlinear optics.

In the linear regime, the intensity at the focal spot of a focused Gaussian beam is given by the laws of Gaussian optics, and depends on the numerical aperture and the input intensity. When power is increased enough, we enter the nonlinear regime, and the optical Kerr effect will self-focus the beam upon itself increasing intensity above the linear prediction. This increase of intensity is counteracted by diffraction, nonlinear losses through multi-photon absorption (MPA) and plasma generation, which will eventually defocus the beam [8].

To overcome these saturating effects the common approach is to strongly focus Gaussian beams with high numerical apertures [9], commonly using microscope objectives. In this way the saturating effects can not decrease intensity fast enough, and the intensity can be increased to the point where the plasma becomes opaque. However these approaches by definition only apply for high numerical apertures and a short working distance, on the order of a few centimeters at best. For longer working distances the laser beam focusing is mainly driven by nonlinear effects, resulting in the formation of elongated dynamic optical structures known as filaments [8]. In Gaussian beam filamentation the intensity is clamped below a saturation level regardless of input power [10, 11]. The physical effect responsible for intensity clamping is indirectly induced by multi-photon ionization (MPI). This process requires nonlinear absorption of energy from the pulse to generate a plasma that will in turn locally decrease the refractive index and defocus the beam. Braun *et al* [12] and Kasparian *et al* [13] defined the clamping intensity as the level for which plasma-and Kerr-induced refractive index changes balance each other. By quantifying this principle, they have established practical criteria to evaluate the clamping intensity from the refractive index coefficient of air, ionization rates for molecules in air and the pulse duration. They find a clamping intensity of $3-4\times10^{14}$ W/cm^2 for propagation in air, which we define as our reference value. Further increasing the power will result in the formation of multiple filaments that grow from beam imperfections, all of which carry roughly the same power and are similarly clamped in optical intensity.

Recent attempts to control nonlinear pulse propagation have suggested the use of periodic potentials [14], and the use of finite energy non-diffracting beams such as Bessel beams [15] and Airy wavepackets [16–18]. Finite energy non-diffracting beams are unique in that they propagate without diffracting over a finite distance, and therefore avoid the classical diffraction vs. Kerr competition seen in Gaussian filaments. The Airy beam in particular exhibits exotic characteristics such as self-

reconstruction [21, 22] and the ability to freely accelerate in the transverse dimension [23]. In addition, Airy wavepackets partially retain their linear characteristics in the nonlinear regime while giving rise to interesting nonlinear properties [19, 20], most notably their resistance to the onset of multiple filamentation at high input powers due to their self-reconstructing abilities.

More recently a cylindrically symmetric version of the Airy beam was proposed [24] and soon after experimentally demonstrated [25]. These peculiar wavepackets, also called ring-Airy beams or autofocusing waves, exhibit an abrupt autofocus in the linear regime and an asymmetric intensity profile along the propagation direction. In this case the focus is formed by the spatial collapse of the rings of the ring-Airy beam, an attribute which arises from the transverse acceleration of the one-dimensional (1D) Airy function [28] when transformed to symmetry. This linear property is not to be confused with the nonlinear mechanism of self-focusing usually associated with Gaussian (or similar) beams propagating in transparent media that exhibit an optical nonlinearity such as the optical Kerr effect. The propagation of nonlinear ring-Airy beams (NLRAB) has been recently investigated theoretically and experimentally in [29] and was found to be fundamentally different from classical Gaussian filamentation, especially concerning the dynamics driving the nonlinear collapse and focal spot.

In this paper we numerically demonstrate that low numerical aperture NLRAB are able to reach higher intensity than the reference value of 4×10^{13} W/cm^2 for a Gaussian beam with the same numerical aperture. We show that the geometry of the ring-Airy beam is of key importance, since it will force the wavepacket into a multiple stage collapse process that is directing energy towards the center in a way never observed before. We show that the driving processes responsible for the overshoot of the above defined reference clamping intensity are the combination of the autofocusing property of the ring-Airy beam and a total internal reflection of light taking place on the inner walls of a self-generated plasma tube. Results presented here are expected to have significant impact on applications where high focal intensities are required to generate stand-off signals, such as white light LIDAR [30], remote LIBS [31], electric discharge triggering and guiding [32], higher harmonic generation [6], THz radiation generation [7] and optical micro-fabrication [33, 34].

II. NUMERICAL MODELS

Two well established numerical models [35] were used in the simulations, an electric field envelope model and a carrier wave resolved field propagator.

The first utilizes an extended non-linear Schrödinger equation [27] that is used to describe the propagation of the envelope $\mathcal{E}(r,t,z)$ of the electric field $E(r,t,z) = \mathcal{E}(r,t,z)e^{i(k_0 z-\omega_0 t)} + c.c.$ of the wavepacket in the z direction in cylindrical coordinates. $\omega_0 = 2\pi c/\lambda_0$ is the central frequency, and $k_0 = 2\pi/\lambda_0$ and $\lambda_0 = 800$ nm are the wavenumber and wavelength of the laser pulse. The propagation equation reads in the Fourier domain:

$$\begin{aligned}\partial_z \mathcal{E}_{k_x,k_y}(\omega,z) = iK_{\omega_0}(\omega,k_x,k_y)\,\mathcal{E}_{k_x,k_y}(\omega,z)\\ +i\frac{\omega}{2\epsilon_0 c^2 \kappa_{\omega_0}(\omega)}\left(\omega P_{k_x,k_y}(\omega,z) + iJ_{k_x,k_y}(\omega,z)\right),\end{aligned} \tag{1}$$

where

$$K_{\omega_0}(\omega,k_x,k_y) \equiv k(\omega) - \kappa_{\omega_0}(\omega) - \frac{k_x^2+k_y^2}{2\kappa_{\omega_0}(\omega)}, \tag{2}$$

and $\kappa_{\omega_0}(\omega) \equiv k_{\omega_0} + k'_{\omega_0}(\omega-\omega_0)$, ω, k_x and k_y denote the Fourier variables corresponding to time t and spatial coordinates x and y, respectively. The first term on the right hand side of Eq. (1) includes all linear effects such as diffraction, dispersion and space-time coupling. The dispersive properties of the medium are described by the full Sellmeier relation $k(\omega)$ for the medium, ϵ_0 is the permittivity of vacuum, and $k'_{\omega_0} \equiv \frac{dk}{d\omega}|_{\omega_0}$.

The terms $P_{k_x,k_y}(\omega,z)$ and $J_{k_x,k_y}(\omega,z)$ account for the nonlinear polarization and current. The frequency multiplying the nonlinear polarization accounts for self-steepening of the electric field envelope $\mathcal{E}(r,\tau,z)$, calculated in the reference frame of the laser pulse $\tau = t - k'_0 z$ in space-time (τ,r,z) in radial symmetry.

The nonlinear polarization of the medium due to the optical Kerr effect is calculated from the pulse envelope by the relation

$$P(\tau,r,z) = 2n_0 n_2 \epsilon_0 |\mathcal{E}|^2 \mathcal{E} \tag{3}$$

where n_0 and n_2 are the linear and nonlinear refractive indexes of the medium respectively.

The current $J_{\omega,k_\perp}$ in Eq. (1) describes plasma absorption and plasma defocussing in the framework of the Drude model by the relation

$$\begin{aligned}J(\tau,r,z) = c\sigma\epsilon_0(1+i\omega_0\tau_c)\,\rho\mathcal{E}\\ +cn_0\epsilon_0\beta_K\left(1-\frac{\rho}{\rho_{nt}}\right)|\mathcal{E}|^{2K-2}\mathcal{E}\end{aligned} \tag{4}$$

where ρ denotes the density of the plasma generated by multi-photon ionization and avalanche. The cross section for inverse Bremsstrahlung, σ, is calculated from the Drude model [40], τ_c is the collision time, and $\beta_K = K\hbar\omega_0\rho_{nt}\sigma_K$ is the cross section for multi-photon absorption with coefficient σ_K for K photons. ρ_{nt} is the density of neutral molecules.

Plasma generation is modeled by the relation

$$\frac{\partial\rho}{\partial t} = \sigma_K|\mathcal{E}|^{2K}(\rho_{nt}-\rho) + \frac{\sigma}{U_i}\rho|\mathcal{E}|^2 \tag{5}$$

where the first term of the right hand side accounts for multi-photon ionization with coefficient σ_K of order $K = 8$ in air, and the second term acounts for avalanche.

$U_i = 12.1$ eV is the ionization potential of oxygen. Recombination of free electrons can safely be neglected since it happens at much longer timescales compared to the pulse duration. More details about the above model can be found in Ref. [8].

The second model utilizes the Unidirectional Pulse Propagation Equation (UPPE) [36] for the full electric field $E(r,t,z)$, also in cylindrical coordinates. Being a spectral solver, the native representation of the field is the form of spectral amplitudes $E_{k_x,k_y}(\omega,z)$ that are functions of the angular frequency ω and the transverse wavenumbers k_x and k_y, computed at every point in z. The scalar equation for the forward propagating field that is used in the simulations reads

$$\begin{aligned} \partial_z E_{k_x,k_y}(\omega,z) &= ik_z E_{k_x,k_y}(\omega,z) \\ +i\frac{\omega}{2\epsilon_0 c^2 k_z}&\left(\omega p_{k_x,k_y}(\omega,z) + i\, j_{k_x,k_y}(\omega,z)\right) \end{aligned} \tag{6}$$

where

$$k_z = \sqrt{k^2(\omega) - k_x^2 - k_y^2} \tag{7}$$

is the propagation constant and $p_{k_x,k_y}(\omega,z)$, $j_{k_x,k_y}(\omega,z)$ are the electric field driven polarization and current density of the material respectively.

Since UPPE is much more expensive computation wise when compared to our envelope model, massive parallelization is necessary in order to solve and post-process large numerical experiments in a practical time-frame. Because of this, we used UPPE mainly to cross-check results obtained by the envelope code and and study electric field related effects.

III. INPUT WAVEPACKET

The input beam has a ring-Airy distribution. The spatio-temporal envelope of the electric field $\mathcal{E}(r,t,z=0)$ is given by Eq.(8)

$$\mathcal{E} = \mathcal{E}_0 \times Ai\left(\frac{r_0 - r}{w_0}\right)\exp\left(\alpha\left(\frac{r_0 - r}{w_0}\right) - \left(\frac{t^2}{t_p^2}\right)\right) \tag{8}$$

where r, and t are the radial and temporal coordinates. Ai is the Airy function [28], $r_0 = 921$ μm is the radius of the main ring, and $w_0 = 61.4$ μm is the scaling parameter of the Airy beam optimized for the most intense focus [24], while $\alpha = 0.05$ is the apodization parameter forcing the beam to be finite in size and energy. In the temporal domain the pulse is Gaussian with a duration of $t_p = 200$ fs at $1/e^2$ radius and a central frequency of 800 nm. The spatio-temporal iso-intensity plot of the input wavepacket used throughout this work is depicted in Fig.1.

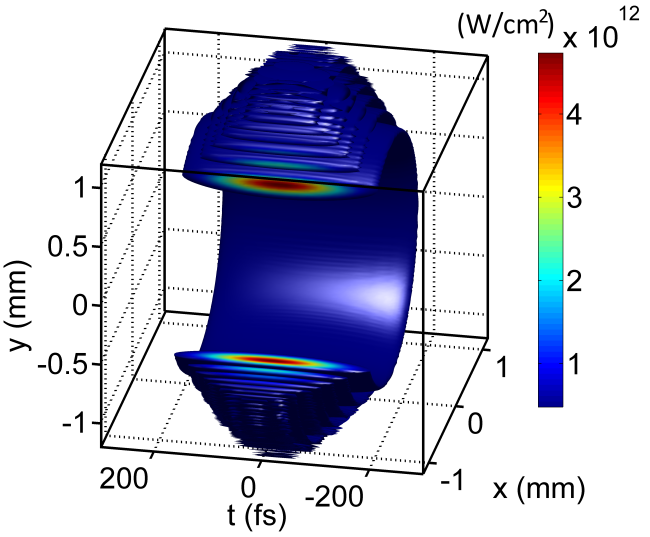

FIG. 1. (Color Online) Iso-intensity of the nonlinear ring-Airy beam in xyt coordinates carrying 24 P_{cr}. The ring-Airy has a radius of $r_0 = 921$ μm (main ring), $w_0 = 61.4$ μm, apodization factor $\alpha = 0.05$, and a duration of $t_p = 200$ fs at $1/e^2$ radius. Isovalue $= 5\times10^{11}$ W/cm^2. Propagation is from left to right.

IV. MODEL OF ATMOSPHERIC AIR

The wavepacket is propagating in air at atmospheric pressure. The nonlinear refractive index of air is taken to be $n_2 = 3.2\times10^{-19}$ cm^2/W [38], which corresponds to a critical power for self-focusing of $P_{cr} = \frac{3.77\lambda_0^2}{8\pi n_0 n_2} = 3.2$ GW [37]. The cross section for multi-photon absorption is $\beta_K = 4\times10^{-95}$cm^{13}W^{-7}, the coefficient for multi-photon ionization is $\sigma_K = 3.4\times10^{-96}$ cm^{16}W^{-8}s^{-1} for $K = 8$ photons at 800 nm using the Keldysh formulation [39] applied to ionization of oxygen with a density of neutral molecules of $\rho_{nt} = 5\times10^{18}$ cm^{-3} and ionization potential of $U_i = 12.1$ eV. Finally the coefficient for inverse Bremsstrahlung $\sigma = 5.5\times10^{-20}$ cm^2 is calculated from the Drude model [40] for a collision time of $\tau_c = 350$ fs. Chromatic dispersion is modeled using the Sellmeier relation for air [41].

While 1D, 2D, and 3D Airy beams (see [16, 19, 22] respectively) can be easily visualized be the reader, cylindrical symmetric Airy beams can be more diffcult. The intensity of a ring-Airy beam (Gaussian in time in this case) can be visualized in xyt space as a series of cocentric rings, each having an Airy distributinion in r, that reduce in amplitude as radius increases as shown in Fig. 1. Temporally, the wavepacket is affected by a variety of effects including chromatic dispersion, self-phase modulation, plasma-induced pulse reshaping, self-steepening and space-time couplings..

The linear autofocusing behavior of the ring-Airy has been well documented in [24, 25]. Due to the transverse acceleration of the Airy profile the beam auto-focuses in the linear regime forming a predictable focus on axis

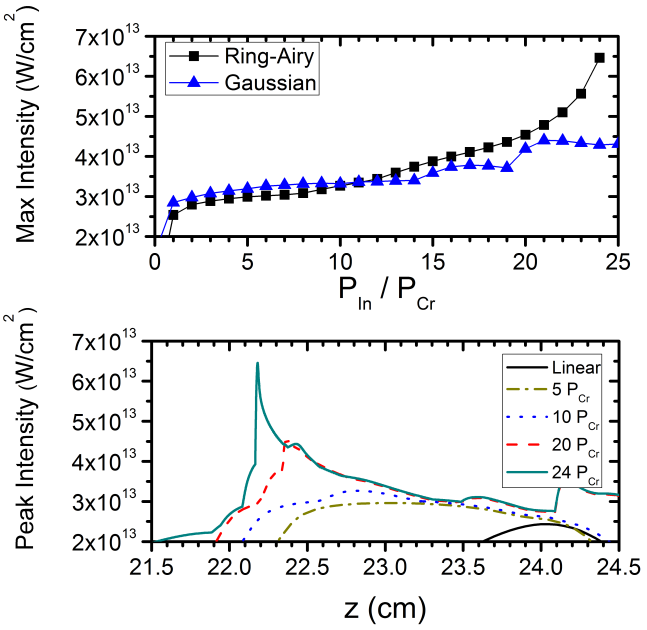

FIG. 2. (Color Online) (a) Peak intensity at the focal spot as a function of total input power for the nonlinear ring-Airy beam (black squares), and Gaussian beam (blue triangles). (b) Peak intensity versus propagation distances close to the focus for various input powers.

as the main ring of the ring-Airy collapses (see Fig.1 of Ref.[24]). The linear ring-Airy beam propagation can be visualized as multiple shrinking rings that increase in intensity as the wavepacket autofocuses. The intensity distribution is asymmetric in z because the rest of the rings of the ring-Airy collapse on-axis further downstream.

V. RESULTS

When the input power is increased to $1P_{cr}$ and beyond, nonlinear effects become observable, modifying the linear auto-focusing behavior of the ring-Airy. In Fig.2(a) we can see the peak intensity at the focus of the NLRAB versus total input power, contrasted with an equivalent envelope Gaussian as defined in Ref.[25] carrying the same power and numerical aperture ($N.A. \simeq 7 \times 10^{-3}$). As we can see the intensity of the Gaussian beam is clamped at the value of $\sim 4 \times 10^{13}$ W/cm^2, in perfect agreement with the reference value estimated in Ref. [13]. We note that this values also agrees with the clamping level estimated from measurements performed with Gaussian beams at the same numerical aperture [26]. In contrast, the NLRAB is increasing in intensity without showing any sign of saturation. At the highest power of $24P_{cr}$ simulated here, the maximum focal intensity ratio between the two beams has reached is 1.5. Further increase of input power are expected to increase this disparity. This is the first time to our knowledge that such high intensity values are predicted for a low numerical aperture of $N.A. \simeq 7 \times 10^{-3}$ at a focal distance of the order of $\sim$ 20 cm, regardless of input power. This finding is of great importance as it shows that even at low numerical apertures, required for long working distances, properly engineered beams allow the remote delivery of intensities above the reference level for Gaussian beams of equivalent numerical aperture. In addition, due to the autofocusing ability of the ring-Airy beam, the focal distance can be easily controlled by choosing the appropriate input beam geometry and power [29], which makes nonlinear ring-Airy beams a much more robust choice than Gaussian beams.

Fig.2(b) shows the peak intensity as a function of the propagation distance in the region of the nonlinear focus of the NLRAB for different input powers. As power is increased, the focus shifts towards the laser source and is increasing in intensity, eventually forming an intense sharp peak at the onset of the focus. The peak itself is well localized in space, and cannot be explained by linear effects and Kerr self-focusing alone, which are acting over much longer length scales in air [19].

To gain insight into this unusual behavior, we monitored in Fig.3 the spatio-temporal (r-t) intensity (first row), generated plasma density (second row) and overall refractive index modulation Δn (third row) of the NLRAB carrying $24P_{cr}$, around the nonlinear focus. The first column shows the r-t distributions of the above mentioned quantities at $z = 22$ cm, before any nonlinear effect becomes significant. In this first stage, which extends from the beginning up to $z = 22$ cm the wavepacket is propagating mostly linearly, and is approaching the linear focus point located at $z = 24$ cm. An on-axis intensity peak forms, surrounded by the shrinking main ring of the NLRAB. This unique intensity distribution generates a plasma by MPI, which can be depictred in the second line of the first column in Fig.3. The plasma generated by the on-axis peak as well as the plasma ring, in this first stage, will both defocus the beam in a way that is indicated by the arrows on the r-t diagram in the first column in Fig.3. The result of this double defocussing process can be seen in the second column of Fig.3, where an intense inner ring is formed in-between the on-axis peak and the main ring of the NLRAB.

This second stage is of key importance, since the intense inner ring will generate an even denser plasma, again through MPI, that has the shape of a tube as it is depicted in the second line of the second column in Fig.3. The plasma tube has a high refractive index contrast with its surroundings and will therefore act as a reflecting interface, resulting in the redirection of light towards the center through total internal reflection. This can be seen in the third stage where the wavepacket collapses ($z = 22.166$ cm) into an intense on-axis peak at $z = 22.18$ cm, depicted in the third and fourth columns of Fig.3. The intense peak eventually breaks up under the effects of MPI and plasma defocussing, a process which takes place over a distance of the order of millimeters.

The reason why intensity increases as power increases is because in this geometry the cylindrical plasma distributions in the first two stages, responsible for the col-

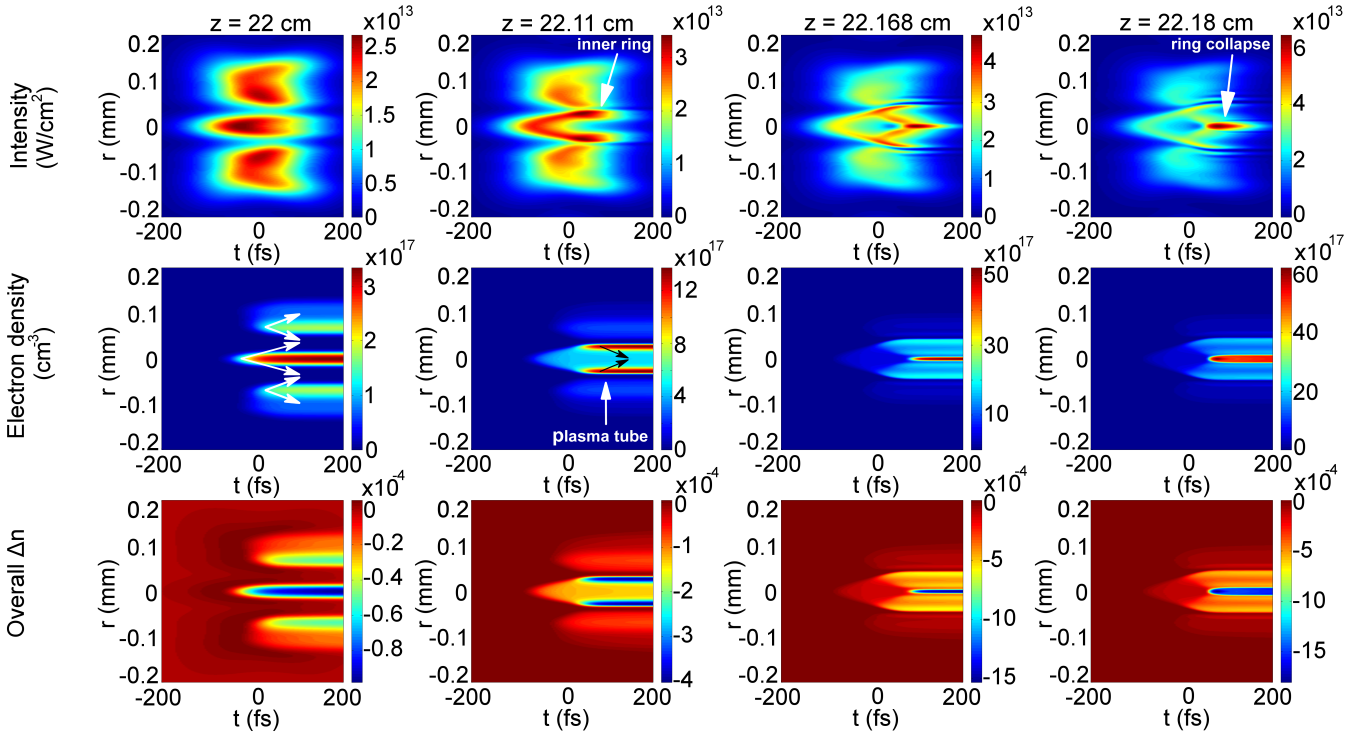

FIG. 3. (Color Online) Spatio-temporal dynamics of the nonlinear ring-Airy beam close to the focus at $z = 22$ cm, 22.11 cm, 22.168 cm, and 22.18 cm (columns 1 to 4). First row: r-t intensity, second row: r-t plasma density, and third row: r-t overall refractive index modulation Δn. Propagation is from right to left. See corresponding movie in the supplementary material online [43].

lapse, are becoming denser as power is increased. In this way more energy is diverted towards the center and intensity can increase further before MPI dominates the third stage. At all stages the strongest effect is associated with plasma, as it is clearly shown in the third row of Fig.3, the overall refractive index modulation $\Delta n(r,t) = \Delta n_{\text{Kerr}} - \Delta n_{\text{Plasma}} = n_2 I(r,t) - \rho(r,t)/2\rho_c$ [42] is almost exclusively negative. A weak positive $\Delta n \sim +10^{-5}$ due to the Kerr effect can be found in the leading part of the pulse, which however is dominated by the much stronger plasma contribution which reaches $\Delta n \sim -4 \times 10^{-4}$ in the second stage and over -7×10^{-3} at the focal spot (third stage).

This complex multiple stage collapse process can also be visualized in the r-z plane using fluence. The radial fluence along propagation in the vicinity of the collapse is shown in Fig.4. The multi-stage process, while not as clearly depicted as in the r-t domain in Fig.3, can still be easily identified. Fig.4 is useful in providing a clear perspective to the degree of localization of the multiple collapse process described in Fig.3. Radially, the collapse is indeed taking place inside a very small space in the center part of the beam. Longitudinally, both stages play out in under 2 mm of propagation distance, which is very short compared to the 22 cm of prior propagation.

The above explanation has been verified by artificially switching off the optical Kerr effect and plasma generation, separately, at the second stage ($z = 22.11$ cm). In the case where Kerr is switched off, shown in Fig.5(b), the wavepacket is still forming the intense on-axis spot, although with slightly less intensity of $\sim 6.2 \times 10^{13}$ W/cm^2, which however is still well over the reference clamping value for Gaussian beams with the same numerical aperture and the whole process remains qualitatively the same. The intensity distribution is almost identical to the case where all effects are accounted for, shown again in Fig.5(a) for comparison. On the other hand when ionization is switched off at $z = 22.11$ cm, shown in Fig.5(c), the wavepacket is not forming the intense sharp peak anymore. Instead it is maintaining a ring-like structure (resembling the one seen in the second column in Fig.3), while slowly self-focusing on itself. Since there is no saturating mechanism present anymore the wavepacket will eventually collapse into a singularity, which however is happening much later along the propagation direction. For completeness, Fig.5(d) shows the r-t intensity distribution at the focal spot when both the Kerr effect and ionization are switched off at $z = 22.11$ cm. Fig.5(c) and Fig.5(d) are almost indistinguishable, further supporting our explanation, further supporting our explanation. From Fig.5 it is clear that the driving physical effect for the formation of the intense peak is plasma formation through MPI, while the Kerr contribution can be considered negligible after the second stage is reached.

Note that the plasma tube in the second stage will partly defocus the beam, however the defocussing strength of the plasma lens is not adequate to induce a

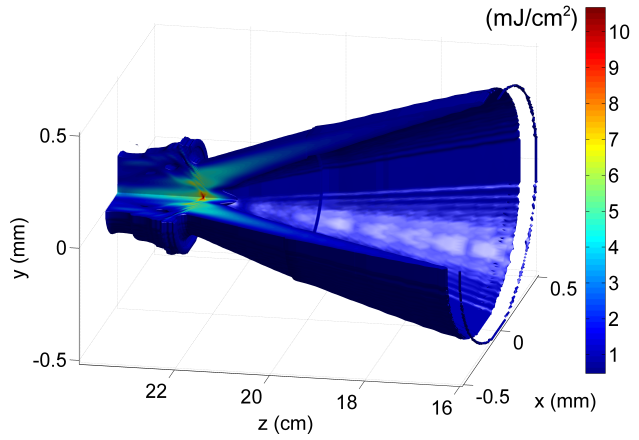

FIG. 4. (Color Online) Radial fluence vs propagation distance at the focal spot of the nonlinear ring-Airy beam. Propagation is from right to left.

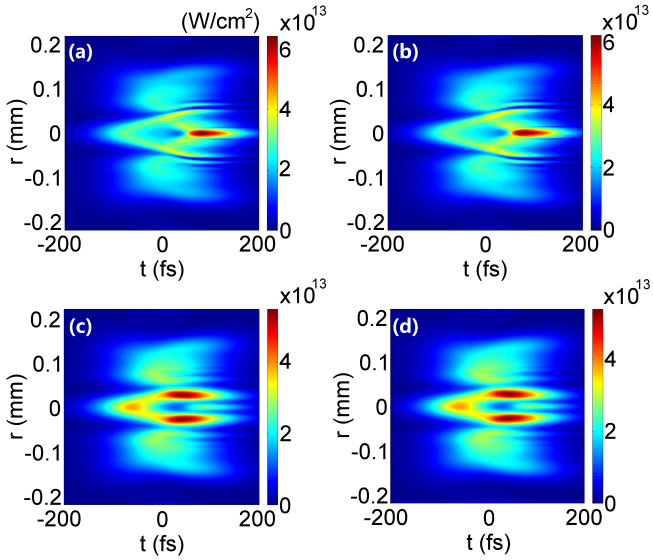

FIG. 5. (Color Online) r-t intensity distribution at the focal spot ($z = 22.18$ cm) for various physical effects switched off at the second stage ($z = 22.11$ cm). (a) All effects taken into account, (b) Kerr effect switched off, (c) MPI switched off, (d) both MPI and Kerr switched off. Propagation is from right to left.

focus 560 μm later. On the other hand the angle for total internal reflection given the refractive index contrast at the edge of the plasma tube is very close to the angle of incidence from on-axis light. For the case depicted in Fig.3 the angle of incidence is $\theta_{rAiry} \simeq 88.563°$, while the angle for total internal reflection is $\theta_{tot} = 88.6°$. This means that almost all light coming from the on-axis spot in the first stage will be reflected towards the center from the plasma tube.

Treating the plasma tube as an interface resembling the interface between the core and cladding of an optical fiber is a safe approximation since the gradient of the refractive index is very steep. Actually, similar results can be obtained if one considers a gradient index, like in GRIN optical fibers. In addition, the effect of plasma absorption on the overall mechanism can be considered negligible since electron densities are more than three orders of magnitude below the critical plasma density of 1.7×10^{21} cm^{-3} at 800 nm. Even in extreme cases that are beyond the scope of this work, the low-absorption region corresponds to the higher refractive index (less plasma), which is where most of the propagation is taking place (inside part of the tube).

Finally, we conducted additional simulations using the UPPE model which is a carrier wave resolved electromagnetic propagator [36]. We verified the findings of the envelope code with only minor quantitative differences between the two models. Most importantly, the multistage plasma assisted collapse mechanism leading to abnormally high intensity values was found to be virtually identical for both codes (results not shown here).

While the UPPE model is much more demanding computation wise, it is on the other hand able to study field related effects such as carrier wave shock formation [4]. Although electric field shocks have never been observed for 800 nm wavelength pulses [44], they have been predicted in regimes of low dispersion and high nonlinearity found at longer wavelengths in various media [3–5]. Assuming a normal dispersion medium, the required laser intensities for shock formation increase as wavelength decreases, and vice versa [5]. Given the reference intensity clamping value of 4×10^{13} W/cm^2, this dependence of the field shock on intensity and wavelength is the main reason why mid and long-IR wavelengths favor field steepening and why shorter wavelengths such as 800 nm do not.

Here we exploit the extremely high intensity reached by the NLRAB to generate an electric field shock in air using a 800 nm wavelength, circumventing the problem of intensity clamping seen in filaments for a given numerical aperture. The reshaping of the electric field can be seen in Fig.6 at $z = 22.2$ cm (red continuous line), when compared to the initial sinusoidal 800 nm waveform (black dashed line). This is the first time to our knowledge, that carrier wave shock formation is predicted in realistically modeled atmospheric air in the near-IR. The reshaping of the 800 nm wavelength electric field is of great importance given the widespread use of Ti:Sapphire lasers in nonlinear optics, and is only one of the many possible applications of the abnormal nonlinear collapse of the NLRAB.

The limit of the mechanism is defined by the lowest of two power thresholds. The first is the maximum plasma density that can be generated in air at the second stage, which is around $\rho_{max} = \rho_{nt}$ when all the oxygen molecules are ionized. If nitrogen is also taken into account, plasma density can increase further by a factor of ~ 4, although the ionization potential of nitrogen is as high as $U_{Ni} = 15.576$ eV. Further increase in input power will lead to a second ionization event of oxygen and nitrogen, and eventually the plasma at the collapse point will become more reflective. The second power threshold is related to the amount of noise in the

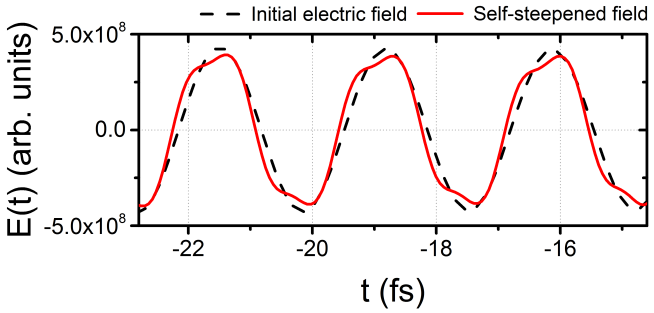

FIG. 6. (Color Online) Electric field reshaping of a 800 nm pulse propagating in air at $z = 22.2$ cm (red continuous line) versus initial unperturbed field (black dashed line) using the UPPE model.

input beam, which at very high input powers will lead to the formation of multiple filaments in the main ring. This will result in the beam breaking up before the first stage can be completed, i.e. the first column of Fig.3 is never reached. This means that the wavepacket will not undergo the multi-stage collapse process, instead it could undergo multiple filamentation having a clamped intensity. However, for the same beam power, Airy beams are mush more robust and resilient to breakup into multiple filaments than Gaussian beams [18, 19, 22]. Airy beams indeed exhibit self-healing properties like Bessel beams. The main limiting factor could therefore be the beam quality (inhomogeneity), potentially lowering the power threshold for observing beam breakup in real experimental settings.

VI. SUMMARY

In conclusion, we have numerically shown, by the use of both envelope and full field propagator models, that NLRAB are able to autofocus up to intensity levels above the reference value for a Gaussian beam with the same NA, and collapse into a single intense on-axis spot. The physical effect that is mainly responsible for this peculiar behavior is the self generated plasma which, due to the geometry of the ring-Airy, is formed in a way that forces the wavepacket into a multiple stage collapse. The collapse process is first initiated by plasma defocussing which results in the formation of a plasma waveguide-like structure, which will in turn redirect light, reflecting it towards the center by means of total internal reflection at a rate greater than saturating mechanisms can compensate. This is the first time to our knowledge that the collapse and intensity increase of a high power wavepacket is actually aided by plasma generation. Results presented here are expected to have significant impact on application that benefit from high focal intensities at low numerical apertures and long working distances [6, 7, 30–34].

Acknowledgments: P.P., D.G.P. and S.T. acknowledge financial support by Laserlab Europe and the Aristeia project FTERA (grant number 2570), co-financed by the European Union and Greek National Funds. In addition, P.P., M.K. and J.V.M. where supported by an Air Force Office of Scientific Research Multidisciplinary University Research Initiative (MURI) grant FA9550-10-1-0561.

[1] C. P. Hauri, W. Kornelis, F. W. Helbing, A. Heinrich, A. Couairon, A. Mysyrowicz, J. Biegert, and U. Keller, Appl. Phys. B **79**, 673 (2004).
[2] C. Hernández-García, J. A. Pérez-Hernández, T. Popmintchev, M. M. Murnane, H. C. Kapteyn, A. Jaron-Becker, A. Becker, and L. Plaja, Phys. Rev. Lett. **111**, 033002 (2013).
[3] P. Whalen, P. Panagiotopoulos, M. Kolesik, and J. V. Moloney, Phys. Rev. A **89**, 023850 (2014).
[4] P. Panagiotopoulos, P. Whalen, M. Kolesik, and J. V. Moloney, Nature Photonics, doi:10.1038/nphoton.2015.125 (2015).
[5] P. Panagiotopoulos, P. Whalen, M. Kolesik, and J. V. Moloney, JOSA B **32**, 8, 1718-1730 (2015).
[6] F. Krausz and M. Ivanov, Rev. Mod. Phys. 81, 163 (2009).
[7] H. G. Roskos, M. D. Thomson, M. Kre, and T. Löffler, Laser & Photonics Review **1**, 349 (2007).
[8] A. Couairon and A. Mysyrowicz, Phys. Rep. **441**, 47 (2007).
[9] P. P. Kiran, S. Bagchi, S. R. Krishnan, C. L. Arnold, G. R. Kumar, and A. Couairon, Phys. Rev. A **82**, 013805 (2010).
[10] W. Liu, S. Petit, A. Becker, N. Akozbek, C. M. Bowden, and S. L. Chin, Opt. Commun. 202, 189 (2002).
[11] A. Couairon, H. S. Chakraborty, and M. B. Gaarde, Phys. Rev. A 77, 053814 (2008).
[12] A. Braun, G. Korn, X. Liu, D. Du, J. Squier, and G. Mourou, Opt. Lett. **20**, 73-75 (1995).
[13] J. Kasparian, R. Sauerbrey, and S. L. Chin, Appl. Phys. B **71**, 877-879 (2000).
[14] M. Bellec, P. Panagiotopoulos, D. G. Papazoglou, N. K. Efremidis, A. Couairon, and S. Tzortzakis, Phys. Rev. Lett. **109**, 113905 (2012).
[15] P. Polesana, M. Franco, A. Couairon, D. Faccio, and P. Di Trapani, Phys. Rev. A **77**, 043814 (2008).
[16] G. A. Siviloglou and D. N. Christodoulides, Opt. Lett. **32**, 979 (2007).
[17] G. A. Siviloglou, J. Broky, A. Dogariu, and D. N. Christodoulides, Phys. Rev. Lett. **99**, 213901 (2007).
[18] D. G. Papazoglou, S. Suntsov, D. Abdollahpour, and S. Tzortzakis, Phys. Rev. A **81**, 061807 (2010).
[19] P. Panagiotopoulos, D. Abdollahpour, A. Lotti, A. Couairon, D. Faccio, D. G. Papazoglou, and S. Tzortzakis, Phys. Rev. A **86**, 013842 (2012).
[20] P. Polynkin, M. Kolesik, J. V. Moloney, G. A. Siviloglou, and D. N. Christodoulides, Science **324**, 229 (2009).
[21] J. Broky, G. A. Siviloglou, A. Dogariu, and D. N. Christodoulides, Opt. Express **16**, 12880 (2008).
[22] D. Abdollahpour, S. Suntsov, D. G. Papazoglou, and S. Tzortzakis, Phys. Rev. Lett. **105**, 253901 (2010).

[23] G. A. Siviloglou, J. Broky, A. Dogariu, and D. N. Christodoulides, Opt. Lett. **33**, 207 (2008).

[24] N. K. Efremidis and D. N. Christodoulides, Opt. Lett. **35**, 4045 (2010).

[25] D. G. Papazoglou, N. K. Efremidis, D. N. Christodoulides, and S. Tzortzakis, Opt. Lett. **36**, 1842 (2011).

[26] F. Theberge, W. W. Liu, P. T. Simard, A. Becker, and S. L. Chin, Phys. Rev. E **74**, 036406 (2006).

[27] T. Brabec, and F. Krausz, Phys. Rev. Lett. **78**, 3282-3285 (1997).

[28] M. V. Berry and N. L. Balazs, American Journal of Physics **47**, 264 (1979).

[29] P. Panagiotopoulos, D. G. Papazoglou, A. Couairon, and S. Tzortzakis, Nat Commun **4** (2013).

[30] J. Kasparian et al., Science **301**, 61 (2003).

[31] S. Tzortzakis, D. Anglos, and D. Gray, Opt. Lett. **31**, 1139 (2006).

[32] R. Ackermann et al., Appl. Phys. B **82**, 561 (2006).

[33] S. Juodkazis, K. Nishimura, S. Tanaka, H. Misawa, E. G. Gamaly, B. Luther-Davies, L. Hallo, P. Nicolai, and V. T. Tikhonchuk, Phys. Rev. Lett. **96**, 166101 (2006).

[34] M. K. Bhuyan, F. Courvoisier, P. A. Lacourt, M. Jacquot, R. Salut, L. Furfaro, and J. M. Dudley, Appl. Phys. Lett. **97**, 081102 (2010).

[35] A. Couairon, E. Brambilla, T. Corti, D. Majus, O. D. Ramirez-Gongora, and M. Kolesik, Eur. Phys. J.-Spec. Top. **199**, 5 (2011).

[36] M. Kolesik and J. V. Moloney, Phys. Rev. E **70**, 036604 (2004).

[37] J. H. Marburger, Prog. Quantum Electron. **4, Part 1**, 35 (1975).

[38] E. T. J. Nibbering, G. Grillon, M. A. Franco, B. S. Prade, and A. Mysyrowicz, J. Opt. Soc. Am. B **14**, 650 (1997).

[39] L. V. Keldysh, Sov. Phys. JETP-USSR (Zh. Eksp. Teor. Fiz. **47**, (1945)) **20**, 1307 (1964).

[40] E. Yablonovitch and N. Bloembergen, Phys. Rev. Lett. **29**, 907 (1972).

[41] E. R. Peck and K. Reeder, J. Opt. Soc. Am. **62**, 958 (1972).

[42] M. D. Feit and J. A. J. Fleck, Journal Name: Appl. Phys. Lett. **24**, 4, 169-172 (1974).

[43] See Supplemental Material at [URL will be inserted by publisher] for a movie of the radial-temporal evolution of intensity and generated plasma vs propagation distance z.

[44] 1. S. B. P. Radnor, L. E. Chipperfield, P. Kinsler, and G. H. C. New, Phys. Rev. A **77**, 033806 (2008).